optica

Deep UV to NIR frequency combs via cascaded harmonic generation in a silica nanowire using nanojoule pulse energies

AKHILESHWAR MISHRA AND RAVI PANT*

Laboratory for Phoxonics and Nonlinear Optics in Nanostructures (PHONON), School of Physics, Indian Institute of Science Education and Research (IISER), Thiruvananthapuram, Kerala 695551, India
**Corresponding author: rpant@iisertvm.ac.in*

Received 20 May 2021; revised 1 August 2021; accepted 2 August 2021 (Doc. ID 432053); published 14 September 2021

Compact, turnkey frequency combs in the deep ultraviolet (UV) to near-infrared (NIR) wavelength region are important for applications ranging from ultralow power spectroscopy and quantum memory to light–atom interactions. Translation of an IR (1550 nm) comb from a compact mode-locked laser (MLL) to visible wavelength region, using cascading of optical nonlinearities, provides the simplest way to realize an on-demand deep UV to NIR comb. However, the translation of an IR comb to the visible region extending from deep UV to NIR has been difficult to achieve in a single device. We exploit chirped pulsed compression and dispersion engineering to report the simultaneous generation of second- (780 nm), third- (520 nm) and sixth-order (260 nm) harmonics of a 1560 nm MLL in a 10 mm long silica nanowire using nanojoule pulse energies. RF spectrum measurements of the 520 nm signal show that the 82 MHz frequency comb at 1560 nm is translated to visible. The use of a single-mode fiber nanotaper and turnkey mode-locked IR laser creates a hybrid platform that provides deep UV to NIR comb and enables applications in quantum optics through trapping and probing of atoms using the evanescent field of nanotaper. © 2021 Optical Society of America under the terms of the OSA Open Access Publishing Agreement

https://doi.org/10.1364/OPTICA.432053

1. INTRODUCTION

Applications such as single-photon dual-comb spectroscopy [1], deep UV spectroscopy [2], and UV excitation of DNA and RNA strands [3] require frequency combs and ultrashort pulse sources extending from near-infrared (NIR) (780 nm) to deep UV (260 nm). Mode-locked lasers (MLLs) in the deep UV to NIR are bulky and require high pump powers and cooling systems. Recent demonstrations of on-chip turnkey MLLs in the infrared (IR) wavelength region around 1550 nm [4] have opened up opportunities for creating compact frequency comb sources in the visible using second- and third-harmonic generation (SHG, THG) [1,5]. However, direct translation of an IR comb to deep UV wavelengths either requires a device with broadband phase matching and strong sixth-order nonlinearity or cascading of nonlinear optical processes in a combination of dispersion-engineered platforms using high energy μJ pulses [6]. While phase matching between the pump and higher-order modes in nonlinear waveguides has been exploited to create combs in the visible, achieving broadband phase matching up to deep UV in a single platform is difficult. Further, small pulse energies of on-chip MLLs (∼nJ) limit cascading of optical nonlinearities required for translating an IR comb to deep UV.

Here, we combine chirped pulsed compression, which has recently been exploited to achieve few-cycle pulses for generating a broadband comb in an all-fiber platform [7], with phase matching between the pump mode and higher-order modes of a single-mode fiber (SMF) taper to achieve cascaded harmonic generation up to the sixth order using nanojoule pulse energies. We simultaneously generate signals at second- (780 nm), third- (520 nm) and sixth-harmonic (260 nm) of a 1560 nm MLL in a single 10 mm long silica nanowire. We use a model that includes the effect of dispersion- and nonlinearity-induced phases [8–12] to calculate the harmonic powers. Using the nonlinear phase shifts obtained from the measured pump powers, we note that chirped pulse compression not only enhances the peak power inside the taper but can also be used to reduce the overall phase mismatch and obtain a good match with the measured harmonic powers. In our experiments, the peak in the harmonic spectrum does not occur exactly at $n\omega_p$, where n is the order of the harmonic and ω_p is the frequency of the peak in the pump spectrum. This behavior can be explained using the interplay between the nonlinear phase shifts and dispersion-induced phase mismatch [10]. The model, therefore, explains the experimental observations qualitatively and quantitatively quite well. Simultaneous generation of frequency combs at 260, 520, and 780 nm in a single nanowire using compact MLLs with nanojoule pulse energies shows the way forward for generating compact visible combs up to deep UV. Generation of deep UV to NIR combs in an all-fiber platform allows guiding of these combs to far-off places by coupling them to low-loss fibers.

We confirm the translation of IR comb to visible through RF spectrum measurements.

2. DISPERSION ENGINEERING

Figure 1 shows a schematic of the setup used for characterizing cascaded harmonic generation in a dispersion-engineered silica nanowire. We use a taper of 900 nm waist diameter in our experiments to achieve phase matching between the optical mode at 1560 nm and the higher-order taper modes at 780, 520, and 260 nm. To arrive at our taper dimensions, we design tapers of different waist diameters and calculate the modal dispersion for different modes present in them. We note that a taper of 900 nm waist diameter provides phase matching of the 1560 nm mode with higher-order modes at 780, 520, and 260 nm in the taper (see Fig. 1 of Supplement 1). For a given taper diameter, mode-locked pulses can undergo broadening or compression on propagation through the taper. Pulse compression or broadening depends on the input pulse parameters and taper dispersion [12]. If the input pulse parameters are such that the pulse experiences compression on propagation through the taper, then it increases the peak power inside the taper. Enhanced peak power and phase matching between the pump mode and higher-order modes inside the taper then results in efficient cascading of optical nonlinearities. Tapering not only provides efficient phase matching through dispersion engineering but also enhances the nonlinearity due to a reduction in the effective mode area (see Fig. 2 of Supplement 1). The enhanced intensity due to pulse compression can improve the phase matching through the nonlinear phase shift [9–11].

Figure 2(a) shows the effective index n_{eff} for different modes of a silica nanowire of waist diameter 900 nm. The effective index (n_{eff}) versus wavelength plots for different modes show that a 900 nm taper provides phase matching between the pump mode at 1560 nm and the higher-order modes at 780, 520, and 260 nm. When we propagate 82 MHz repetition rate mode-locked pulses, centered at 1560 nm, through this nanowire, we simultaneously observe SHG (780 nm), THG (520 nm) and CSHG (260 nm) (see Fig. 1). We attribute the signal at 260 nm to the second harmonic of the third-harmonic signal at 520 nm and therefore, we label it as CSHG.

Figure 2(b) shows the β_1 versus wavelength plots for the pump, SHG, and THG modes, where β_1 is the inverse of the group velocity. Both the SHG and THG signals have larger β_1 compared to the pump mode and therefore propagate more slowly compared to the pump, which results in pulse walk-off. From Fig. 2(b), we further note that the slope of β_1 for THG has an opposite sign compared to the pump signal. For a negatively chirped pulse, which is typically used in our pulse propagation simulations to match the input pulse profile (see Fig. 3 of Supplement 1), the THG signal experiences broadening compared to the pump. The broadening of the THG signal pulse helps in reducing the pulse walk-off and improving THG efficiency. Figure 2(c) plots the calculated group velocity dispersion (GVD) parameter D as a function of wavelength. The GVD parameter for the optical modes at the pump (black), SHG (red), and THG (green) signal matches closely with each other.

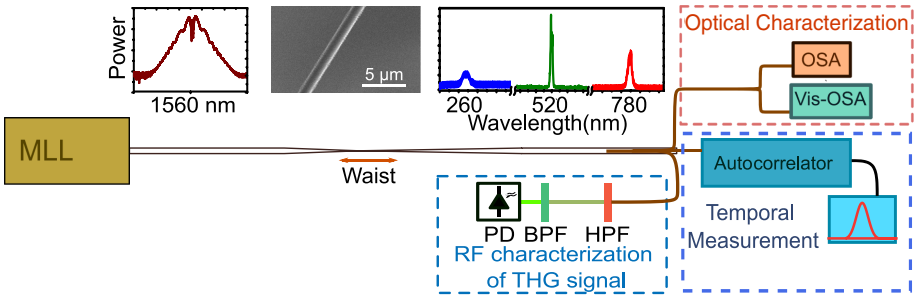

Fig. 1. Schematic of cascaded harmonic generation in a silica nanowire. Setup for the generation and characterization of cascaded harmonics in a single silica taper. Mode-locked pulses from an erbium fiber laser are coupled to the nanotaper. Optical and RF spectra are analyzed using photodetectors and spectrum analyzer. Input and output pump pulses are characterized using an autocorrelator. The inset shows the SEM image of a taper with 900 nm waist diameter. MLL, mode-locked laser; OSA, optical spectrum analyzer; HPF, high-pass filter; BPF, bandpass filter; PD, photodiode.

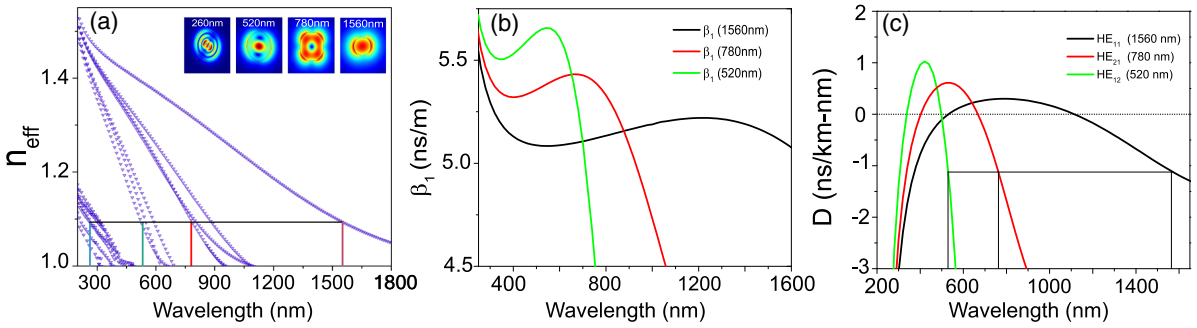

Fig. 2. Dispersion engineering for the cascading of optical nonlinearities in a silica nanotaper. (a) Effective refractive index n_{eff} versus wavelength for a 900 nm nanotaper showing phase matching of the fundamental mode at 1560 nm to the higher-order modes at 780, 520, and 260 nm; (b) simulated β_1 values for the pump (black), SHG (red), and THG (green) modes as a function of wavelength; (c) GVD parameter D for the pump mode (black, HE_{11}), SHG mode (red, HE_{21}), and the THG mode (green, HE_{12}), showing that D is nearly the same for the three modes.

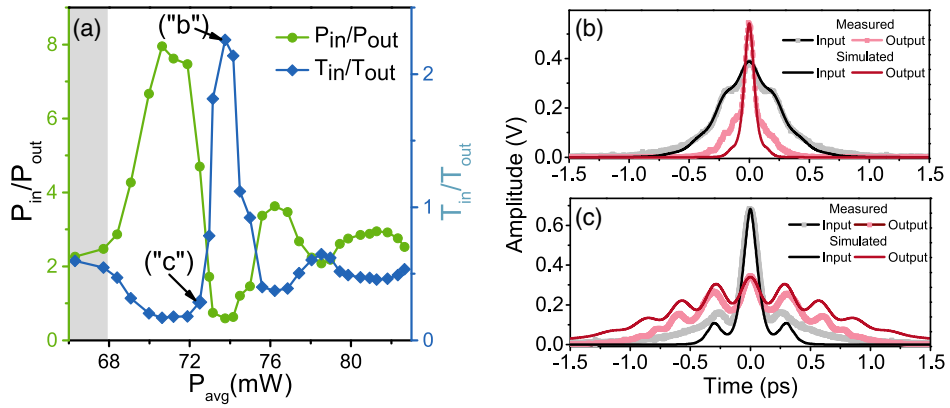

Fig. 3. Pulse control for the cascading of optical nonlinearities in a silica nanotaper. (a) Ratio T_{in}/T_{out} (diamonds) of the pulse widths at the input (T_{in}) and output (T_{out}) of the nanotaper. The gray shaded region shows the Q-switched regime of the MLL. Pulse widths and average powers at the input and output of the taper are used for calculating the corresponding peak powers P_{in} and P_{out} and to plot the ratio P_{in}/P_{out} (dots). (b) Measured (symbols) and simulated (solid lines) autocorrelation traces for the pulses at the input and output of the nanotaper, corresponding to point "b" in panel (a), where the pulse has the highest generation for all the harmonics; (c) measured (symbols) and simulated (solid lines) autocorrelation traces for the input and output pulses corresponding to point "c" in panel (a) for which the input peak power is the maximum.

3. EXPERIMENTAL DESIGN AND MEASUREMENTS

We use a Vytran glass processor to make tapers of different diameters from an SMF (Corning SMF28e). The Vytran glass processor is capable of drawing tapers up to 10 μm waist in a single run with an accuracy of 1 μm. We fabricate a taper with a 10 mm long waist and 30 mm long up- and down-transition regions to achieve adiabatic coupling for maintaining low loss. We then retaper the waist to obtain the required dimensions. This process allows a good diameter control, as the scaling factor is fixed during the retapering of the waist. This taper drawing technique is quite robust, as we observe all the harmonic signals, with quite repeatable efficiencies, every time we make the taper and repeat the experiments. Prepared tapers are then mounted on a holder to keep them taut and straight. Mode-locked pulses from an erbium fiber laser (Pritel femtosecond fiber laser) with a repetition rate of 82 MHz are then launched into the taper. For the MLL, the pulse profile and width are found to be dependent on the pump laser current. The measured pulse widths for the average powers of 66.3, 72.5, 73.7, 79.2, and 82.6 mW are 630, 140, 486, 211, and 224 fs, respectively. The transmitted IR pump is coupled to an optical spectrum analyser (OSA: Yokogava AQ6375B) to measure the input and output pulse spectrum. A visible spectrometer (Ocean Optics Maya) is connected directly at the output of the taper to observe the SHG, THG, and CSHG spectra at different pump powers. To simultaneously observe the SHG, THG, and CSHG spectra, we use an acquisition time of 100 ms, and the output pigtail end is in contact with the input slit of the spectrometer. However, for this condition THG signal saturated the CCD detector in the visible spectrometer (see Fig. 4 of Supplement 1), and so the power of the THG signal was measured directly on a power meter (Thorlabs S120VC) using a bandpass filter. To avoid detector saturation from the THG signal, we measure the THG spectra using a much smaller acquisition time (13 ms) and keep the fiber at a fixed distance away from the input slit of the spectrometer. Input and output pulses are characterized using Femtochrome FR-103XL Autocorrelator. The RF spectrum of the pump is measured using a 10 GHz bandwidth IR photodiode (EOT ET5000F) and an RF spectrum analyzer (RFSA) (Rhode and Schwartz FSU43). For measuring the RF spectrum of the THG signal, we couple the green light through an IR blocking filter and green bandpass filter to a Si photodiode (Thorlabs PDA10A2) and observe the beat signal on the RFSA.

4. RESULTS

A. Pulse Control

To study the effect of pulse control on the harmonic generation, we propagate pulses with different input pulse profiles through our tapers (see Fig. 3 of Supplement 1). Pulses with different input profiles are obtained as we increase the power of the erbium fiber MLL. We attribute the variation of the input pulse profile with the pump power to different chirps induced in the MLL [13]. We measured the pulse width at the input and the output of the taper using an autocorrelator. For the input pulse measurement, we use a 25 cm long patch cord that has a similar length as the input untapered region of the tapered fiber. We measure the output pulse width directly from the tapered fiber end. We measure the average power using the power meter at the input and output of the taper. With the knowledge of pulse width and average power we have calculated the peak powers of the input and the output pulses. Figure 3(a) plots the ratio T_{in}/T_{out} (diamonds) of the input (T_{in}) to output (T_{out}) pulse widths along with the ratio P_{in}/P_{out} (dots) of the input (P_{in}) to output (P_{out}) pulse peak powers, at the pump wavelength, as a function of the average input pump power P_{avg}. Point "b" in Fig. 3(a) corresponds to P_{avg} of 73.7 mW, at which the maximum generation occurs for all the harmonics. For $P_{avg} = 73.7$ mW, the ratio T_{in}/T_{out} achieves a maximum value of ~2.3 [see point "b" in Fig. 3(a)], which shows that the pulse at the output of the taper is compressed by a factor of >2 [see Fig. 3(b)]. The pulse compression increases the peak power P_0 inside the nanowire, which reduces the ratio P_{in}/P_{out} to ~0.5 at 73.7 mW [Fig. 3(a)]. The point labeled "c" ($P_{avg} = 72.5$ mW) in Fig. 3(a) corresponds to a pulse with the maximum peak power at the input of the taper. Symbols and solid lines in Figs. 3(b) and 3(c) show the measured and simulated autocorrelation traces for the input and output pulses, respectively. For the input pulse corresponding to the maximum P_{in}, pulse broadening reduces the peak power P_0 inside the nanowire [see Fig. 3(c)]. The reduced P_0 then results

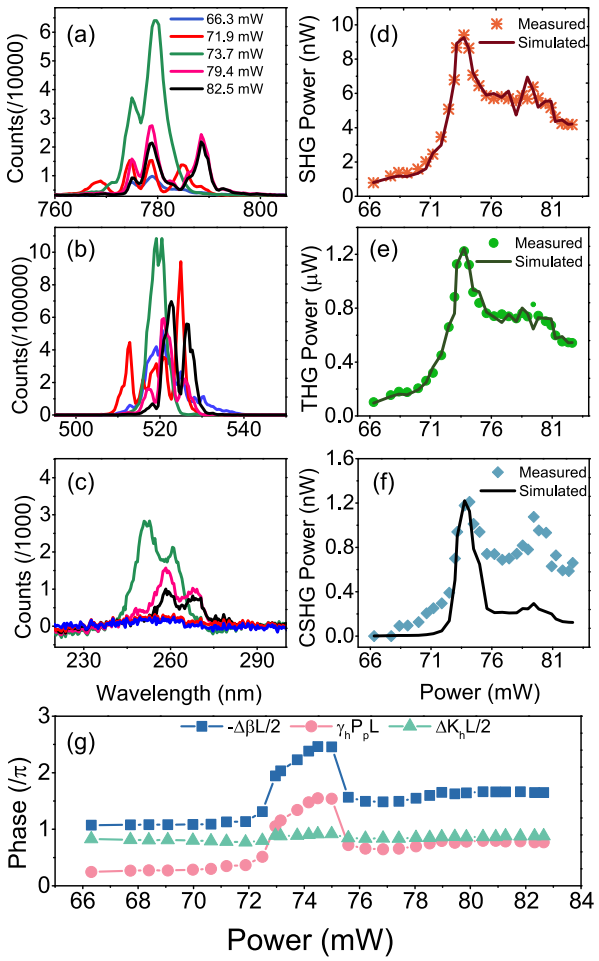

Fig. 4. Visible optical spectra and harmonic powers for different pump powers. (a)–(c) Measured optical spectra for the second-, third- and cascaded second-harmonic signals, respectively, at different pump powers. Spectrum in (b) has been scaled by a factor of 120 to show actual power relationship between the spectra (a)–(c). (d)–(f) Simulated (lines) and calculated (symbols calculated from the measured spectra) powers in the SHG, THG, and CSHG signals, respectively, as a function of the pump power P_{avg}; (g) overall phase mismatch ($\Delta K_h L/2$) as a function of input pump power after the compression of the pulse (green); dispersion-induced phase shift ($-\Delta\beta L/2$) (blue); and intensity-dependent phase shift (γPL) (pink), where $\Delta K_h L/2 = -\Delta\beta L/2 - \gamma_h PL$.

in decreased harmonic efficiency. For other values of P_{avg}, the pulses broaden by a factor of ≥ 2 on propagation through the taper [see diamonds in Fig. 3(a)], which reduces the peak power inside the taper, compared to the value at $P_{avg} = 73.7$ mW [Fig. 3(b)]. Through the input pulse control, it is, therefore, possible to enhance the peak power inside the taper for the cascading of optical nonlinearities.

To simulate pulse propagation, we use the split-step Fourier method and consider only the waist region of the taper. Since the input untapered part has a length similar to the patch cord, which is used for measuring the pulse width, we did not include it in the pulse simulations in Figs. 3(b) and 3(c). For the transition region at the input of the taper, we calculate L_D and L_{NL} using the smallest measured input pulse width of ~140 fs (full width at half-maximum) for which the peak power P_{in} is also close to the highest peak power (~6.3 kW) used in the experiments. Since the GVD β_2 and nonlinearity parameter γ vary along the transition region, we use their largest calculated values in the region (at the 5 μm taper diameter) to calculate L_D and L_{NL} (see Supplement 1 Table 1). Both L_D and L_{NL} achieve the smallest values of 6.1 cm and 2 cm, respectively, in the transition region part (125 μm to 5 μm diameter). From Fig. 2 of Supplement 1, which plots the variation of the effective mode area and the GVD parameter with taper diameter at the pump wavelength, it is also evident that both β_2 and γ increase as we approach the waist. Since L_D and L_{NL} are larger than the physical length of the transition region, we have neglected the input transition region in our simulations. For the waist region, we obtain L_D and L_{NL} of 4.5 and 3 mm, and therefore only the taper waist is included in the pulse propagation simulations. For L_D and L_{NL} in the output transition region and untapered part to be comparable to the physical length of these regions, pulses have to undergo large compression in the waist so that the pulse width reduces and the peak power increases to make both L_D and L_{NL} comparable to propagation lengths of these parts. We did not observe such large compression factors in our measurements. We have therefore neglected the effect of the output transition region and untapered part also. Since the effect of the input transition region on pulse propagation is minimal, it will not affect the harmonic generation in the waist.

B. Harmonics Characteristics

Figures 4(a)–4(c) show the measured optical spectra for the SHG, THG, and CSHG signals at 780, 520, and 260 nm, respectively, at different MLL powers. As mentioned in the experimental design section, the simultaneous acquisition of the SHG, THG and CSHG spectra saturated the detector at the THG wavelength (see Fig. 4 of Supplement 1). The THG spectra in Fig. 4(b) are, therefore, obtained using a smaller acquisition time [see Fig. 4(a) of Supplement 1], whereas the spectra in Figs. 4(a) and 4(c) are measured under the same condition as in Supplement 1, Fig. 4(b). To show the actual power relationship between different harmonics, we have, therefore, scaled the y axis of Fig. 4(b) by the ratio ($A_{THG}/A_{SHG} \sim 120$) of the spectral areas of the THG (A_{THG}) and SHG (A_{SHG}) signals, obtained using Fig. 4(a) of Supplement 1. As mentioned earlier, the power of the THG signal was also measured directly on a power meter using a bandpass filter centered around 520 nm. From the measured optical spectra at different pump powers and using the directly measured THG signal power, we calculated the powers of the SHG and CSHG signals (see Supplement 1, Section S3). The SHG (*), THG (circles) and CSHG (diamonds) signal powers are plotted in Figs. 4(d)–4(f), respectively. We achieve the maximum powers of ~10 nW, 1.2 μW, and 1.2 nW for the SHG, THG, and CSHG signals, respectively, at $P_{avg} = 73.7$ mW. Since the second-harmonic efficiency and thus power is small in silica, it is, therefore, difficult for the SHG signal to generate a third harmonic at 260 nm with 10% efficiency. We, therefore, attribute the 260 nm signal to be the second harmonic of the third-harmonic signal at 520 nm, which has much higher power than the SHG signal at 780 nm. The signal at 260 nm is therefore labeled as the CSHG.

For all the harmonics, we achieve the maximum powers for the input pulse corresponding to $P_{avg} = 73.7$ mW at which the maximum pulse compression occurs in the nanowire. The maximum efficiency at $P_{avg} = 73.7$ mW occurs due to two reasons: (i) increased pulse intensity due to pulse compression [Fig. 3(b)] and (ii) compensation of the dispersion-induced phase mismatch through the nonlinearity-induced phase, as seen from Eqs. (1)–(3).

We use Eq. (2) to simulate the powers of the SHG and CSHG in Figs. 4(d) and 4(f), respectively, and Eq. (3) to simulate the THG power in Fig. 4(e).

While even-order nonlinearities are absent in silica due to its centrosymmetric nature, SHG has been predicted and observed in silica fibers exploiting the surface nonlinearities and photogalvanic effect [12,14–17]. SHG due to the photogalvanic effect requires fibers with specific dopants and fiber illumination using high-energy pulses for the formation of photoinduced gratings, which provide phase matching for SHG [15,17–19]. Since the strength of the photo-induced grating increases with time, the SHG signal due to the photogalvanic effect increases with time [15,16,18,19]. We did not observe any change in the measured SHG power over a period of 12 h. SHG due to surface-induced nonlinearities and multipole contributions have been predicted in fiber tapers [20]. Therefore, we attribute SHG in our nanowires to the surface- and multipole-induced nonlinearities, which occur in tapers due to the symmetry breaking at the surface and high field intensity due to the small mode area [16,20]. We use the coupled differential equations for the evolution of pump (A_p) and SHG (A_s) field envelopes [see Eqs. (3)–(9), Supplement 1, Section S4] [12] and combined them with the surface nonlinearity-induced contribution to obtain the SHG power P_s [see Supplement 1, Eq. (10)] as [12]

$$P_s = \gamma_{\mathrm{SH}}^2 P_p^2 L^2 \left[\frac{\sin^2[(\kappa - 2(\gamma_s - \gamma_p)P_p)L/2]}{[\kappa - 2(\gamma_s - \gamma_p)P_p]^2 (L/2)^2}\right]. \quad (1)$$

Here γ_{SH} is the nonlinearity parameter based on the contribution of surface nonlinearity and bulk multipole contribution [20], $\kappa = n_s\omega_s - 2n_p\omega_p$ is the wavenumber mismatch, $\gamma_s = \eta(2\omega_p n_2(\omega_s))/(c\,A_{\mathrm{eff}}(\omega_p))$ is the Kerr nonlinearity parameter responsible for cross-phase modulation (XPM) at the SHG frequency ω_s, and η is the scaling factor to account for the mode overlap, which is estimated to be 0.7 for SHG. $\gamma_p = (\omega_p n_2(\omega_p))/(c\,A_{\mathrm{eff}}(\omega_p))$ is the Kerr nonlinearity parameter contributing to self-phase modulation (SPM) at the pump frequency ω_p. Here $n_2(\omega_{p,s})$ is the nonlinear refractive index, and $A_{\mathrm{eff}}(\omega_p)$ is the mode area at the pump frequency.

From Eq. (1), we see that the SHG power depends on the dispersion- and nonlinearity-induced phase mismatch. When $\kappa = 0$ and the nonlinearity-induced phase shift is neglected, perfect phase matching occurs. In this case, the SHG signal will appear exactly at twice the pump frequency. However, in the presence of SPM- and XPM-induced phase shifts, the SHG signal frequency will shift from $2\omega_p$ to a frequency $\omega \simeq 2\omega_p$ for which κ has a nonzero value, such that it minimizes the overall phase mismatch due to dispersion and nonlinearity.

Using the nonlinear refractive index values $n_2(\omega_{p,s})$ at the pump and SHG frequencies [21], we obtain $\gamma_s = 0.113$ W^{-1} m^{-1} and $\gamma_p = 0.053$ W^{-1} m^{-1}. Using $\Delta\beta_1$ value from Fig. 2(b), we obtain a pulse walk-off length ($L_w^{\mathrm{SH}} = \frac{T_0}{\Delta\beta_1}$) of 0.83 mm for a pulse width (T_0) of 250 fs, where $\Delta\beta_1$ is the inverse of the group velocity mismatch. For a peak power P_p of 7 kW, the XPM length ($L_{\mathrm{xpm}}^{\mathrm{SH}} = \frac{1}{2\gamma_s P_p}$) is 0.63 mm, and the SPM length ($L_{\mathrm{spm}}^{\mathrm{SH}} = \frac{1}{\gamma_p P_p}$) is 2.7 mm. We can see that $L_{\mathrm{xpm}}^{\mathrm{SH}}$ is smaller than L_w^{SH}, whereas $L_{\mathrm{spm}}^{\mathrm{SH}}$ is almost 3 times L_w^{SH}. We have therefore ignored the SPM-induced phase shift in our model to obtain

$$P_s(L) = |\gamma_{\mathrm{SH}} P_p L|^2 \mathrm{sinc}^2(\Delta \mathrm{K_s} L/2), \quad (2)$$

where the overall effective wave vector mismatch $\Delta K_s = \kappa - 2\gamma_s P_p$ includes the effect of the dispersion κ and the XPM $2\gamma_s P_p$. We use the measured THG signal power at 520 nm as the input pump power for simulating the CSHG signal power at 260 nm. In Figs. 4(d) and 4(f), we have plotted the simulated power (solid lines) with the measured powers for SHG and CSHG (symbols). For fitting Eq. (2) to the experimentally obtained SHG powers in Fig. 4(d), we use the measured pump powers to calculate the XPM-induced phase shifts and tuned the value of κ to get the best fit at each pump power. For fitting Eq. (2) to the data in Fig. 4(f), we have assumed perfect phase matching because THG pump power for generating deep UV signal at 260 nm is small and therefore the XPM-induced phase shift is neglected. Further, the density of higher-order optical modes near 260 nm is large, so there is a higher possibility of finding a mode with perfect phase matching. We use a γ_{SH} parameter value of 0.2 W$^{-1/2}$ m^{-1} from [20] for fitting to the measured SHG power in Fig. 4(d). The nonlinear parameter γ_{SH} increases with the wavelength according to $\frac{1}{\lambda^3}$ [20]. For a 520 nm pump, which is used for 260 nm signal generation through CSHG, we expect γ_{SH} to be at least 27 times the value used for fitting the SHG data. For fitting the calculated 260 nm powers to the measured values in Fig. 4(f), we use $\gamma_{\mathrm{SH}}^{520} = 12$ W$^{-1/2}$ m^{-1}, which is 60 times larger than γ_{SH} rather than 27 times, as we expected. We attribute this variation to larger values of second-order nonlinear refractive index at 520 nm and to the fact that pump mode field diameter at 520 nm may be lower by more than 3 times, which is used in arriving at $1/\lambda^3$ dependence. From Fig. 4(f), we see that the simulated 260 nm signal power fits well to the measured power (diamonds) and follows the square of the measured THG pump power in Fig. 4(e), as expected for perfect phase matching.

To fit the THG signal power $P_{\mathrm{TH}}(L)$ in Fig. 4(e), we obtain the $P_{\mathrm{TH}}(L)$ at the output of the nanowire according to (see Supplement 1, Section S4) [12],

$$P_{\mathrm{TH}}(L) = |\gamma_{\mathrm{TH}} L|^2 P_p^3 \mathrm{sinc}^2(\Delta \mathrm{K_h} L/2). \quad (3)$$

Here $\Delta K_h = -\Delta\beta - 2\gamma_h P_p$ is the overall phase mismatch per unit length, $\Delta\beta = n_h\omega_h - 3n_p\omega_p$ is the dispersion-induced wave vector mismatch, $n_{h,p}$ are the effective refractive index of the THG (h) and pump (p) modes, respectively, and $\gamma_h P_p$ is the contribution of nonlinearity to the overall ΔK_h. The nonlinearity parameter γ_{TH} is responsible for THG and is equal to 0.0011 W^{-1} m^{-1}. For γ_{TH}, the mode overlap factor η is estimated to be 0.03 from Ref. [22]. $\gamma_h = \eta(3\omega_p n_2(\omega_h))/(c\,A_{\mathrm{eff}}(\omega_p))$ is the nonlinearity parameter for XPM at the THG frequency, and η for THG is estimated to be 0.5. As in the case of SHG, we have ignored the pump SPM contribution to THG pulse because γ_h (0.14 W^{-1} m^{-1}) is almost 3 times higher than γ_p. Further, the L_w^{TH} walk-off length for THG is 0.54 mm, $L_{\mathrm{xpm}}^{\mathrm{TH}}$ is calculated to be 0.48 mm, whereas $L_{\mathrm{spm}}^{\mathrm{TH}}$ is 2.7 mm. Since $L_{\mathrm{xpm}}^{\mathrm{TH}} < L_w^{\mathrm{TH}}$, we only consider the XPM-induced phase shift in our simulations, as explained in the discussion following Supplement 1, Eq. (16). In [10], Zheltikov *et al.* noted that due to the dispersion- and nonlinearity-induced phase shifts, the peak of the THG signal spectrum may not occur exactly at $3\omega_p$, where ω_p is the frequency of the maxima in the input pulse spectrum. We also observe that the peak of the THG spectrum does not occur exactly at $3\omega_p$, (see Supplement 1, Fig. 5). This shift of the THG frequency, as described earlier, is attributed to the nonlinear phase shift introduced by XPM from the pump. From Fig. 5 of Supplement 1, we

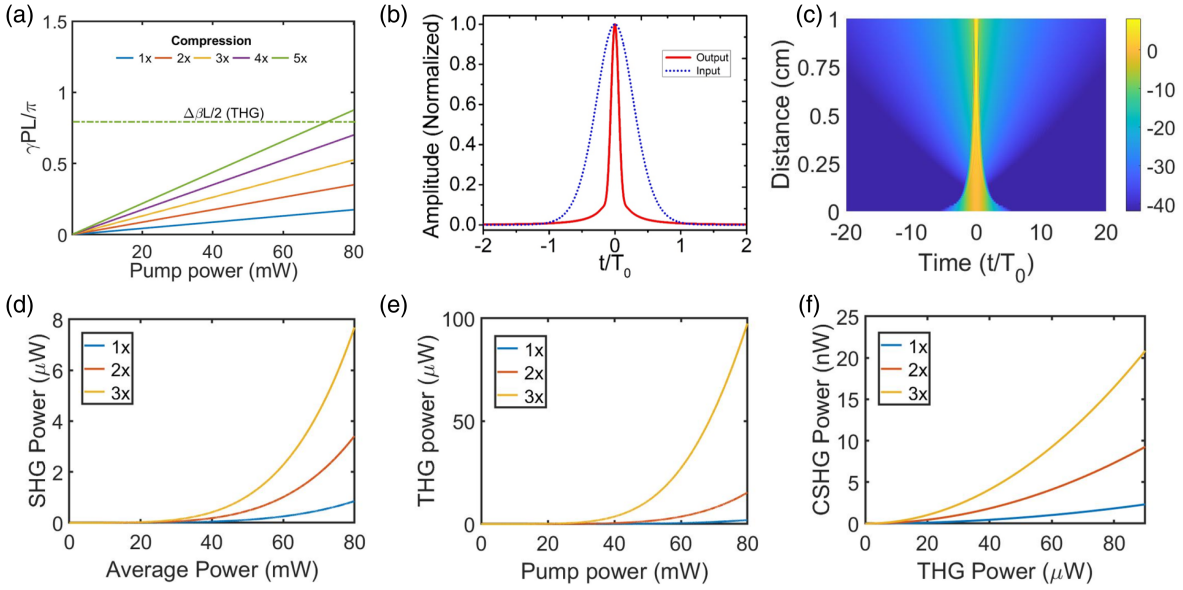

Fig. 5. Simulations using optimized pulse parameters parameters (a) Nonlinear phase shift as a function of the input pump power for different pulse compression factors; (b) input (blue) and the output (red) pulse autocorrelation; (c) evolution of the chirped pulse along the taper length to achieve a compression of the pulse by a factor of 5.6; (d) simulated SHG power as a function of the input pump power for different pulse compression factors; (e) simulated THG power as a function of the input pump power for different pulse compression factors; (f) CSHG power as a function of the THG power generated in the taper; third-harmonic power from (e) is used as the pump for CSHG power calculation.

see that there is a negative shift in the wavelength of the THG signals ($\omega_h^{\text{peak}} < 3\omega_p^{\text{peak}}$). From Fig. 2(a), we note that $\omega_h^{\text{peak}} < 3\omega_p^{\text{peak}}$ results in $n_h\omega_h$ to be smaller than $3n_p\omega_p$, making $\Delta\beta$ negative. The negative value of $\Delta\beta$ will compensate for the XPM-induced phase as the value of $-\Delta\beta$ becomes positive, thus reducing the overall phase mismatch. The fitted value of $-\Delta\beta L/2$ is shown in Fig. 4(g), along with the values of $\Delta K_h L/2$ and $\gamma_h P_p L$. We note that the pump-induced XPM can give rise to an asymmetric pulse due to the difference in the group velocity of the pump and signal. Since the pump is moving faster than the signal, we expect the leading edge of the signal to see a higher conversion rate compared to the trailing edge.

As can be seen from Figs. 4(d)–4(f), our model involving Eq. (2) for SHG and CSHG, and Eq. (3) for the case of THG, closely matches with the measured power of the harmonics. From Eqs. (2) and (3), we see that both dispersion (κ & $\Delta\beta$) and nonlinearity ($\gamma_{s,h} P_P$) contribute to the overall phase shift $\Delta K_{h,s} L/2$. Pulse compression, therefore, provides higher efficiency through increased intensity in the nanowire, minimizing phase mismatch.

Figure 4(g) plots the overall phase mismatch ($\Delta K_h L/2$) for the THG in (green) and the contributions from the dispersion-induced phase ($-\Delta\beta L/2$) (blue) and nonlinearity-induced phase ($\gamma_h P L$) (pink) (see Supplement 1, Section S4). From Fig. 4(g), it is evident that the pulse compression compensates for the dispersion-induced phase mismatch $\Delta\beta L$ to achieve lower overall phase mismatch $\Delta K_h L/2$. While the overall phase mismatch $\Delta K_h L/2$ is smaller for the pump powers, where no pulse compression occurs, the combined effect of enhanced intensity and reduced phase mismatch results in higher harmonic power for the pump powers at which pulse compression occurs. For fitting the simulated power to the measured harmonic power in Figs. 4(d)–4(f), we use the dispersion-induced phase as a fitting parameter. Different values of dispersion-induced phase are used for fitting to take into account the changes in pump pulse parameters, which shift the peak of the pump pulse spectrum and cause a deviation in the frequency of a harmonic signal peak from $n_0\omega_p$, where n_0 is the order of the generated harmonic (see Supplement 1, Fig. 5).

Since chirped pulse compression enhances the efficiency of harmonic generation through nonlinearity-induced phase and enhanced intensity in the nanowire, we study the effect of pulse compression on nonlinear phase shift and harmonic power generation. Figure 5(a) plots the nonlinear phase shift as a function of the input pump power for different amounts of pulse compression seen by an input pulse of fixed pulse width. The dispersion-induced phase mismatch $\Delta\beta L/2 \sim 0.8\pi$ in Fig. 5(a). As the pulse compression increases, higher nonlinear phase shift occurs for a given input pump power, which helps in better compensation of the dispersion-induced phase mismatch $\Delta\beta L/2$ [see Fig. 5(a)]. We use pulse compression factors up to 5, which can be generated by chirping the input pulse [23]. Figure 5(b) shows the simulated input and output autocorrelation traces for an input secant hyperbolic pulse of pulse width 150 fs, input peak power 7 kW (pulse energy 1 nJ), and a chirp parameter of -5. On propagation through the nanowire, the pulse compresses by a factor of 5.6 [see Fig. 5(b)]. The pulse evolution along the length of the nanowire is shown Fig. 5(c). From Fig. 5(c), we note that by tuning the chirp parameter, we can compress the pulse in our nanowire and keep the pulse width nearly the same throughout the propagation length. To study the effect of different pulse compression factors on the harmonic power generation, we plot the powers for the SHG, THG, and CSHG signals in Figs. 5(d)–5(f), respectively, using Eqs. (2) and (3). We have used a taper waist length of 1 mm in our simulations; here, as for longer lengths, we get very large conversion efficiencies for THG and SHG and pump depletion can no longer be ignored and the model is no longer valid. We use an input pulse width of 150 fs and $\Delta\beta L/2 = \pi$ for the simulations in Figs. 5(d) and 5(e). For calculating the CSHG power in Fig. 5(f), we use the THG power from Fig. 5(e) as the pump

power and neglected the dispersion-induced phase mismatch because there are many modes available for phase matching [see Fig. 1(a)]. We have taken γ_{SH} to be 2.5, which is taken from [20] for TE_{01} mode. From Figs. 5(d)–5(f), we see that the harmonic power increases with the pulse compression factor due to the combined effect of enhanced pump intensity inside the nanowire and the compensation of the dispersion-induced phase mismatch by the nonlinearity-induced phase. While we achieve SHG and THG with maximum conversion efficiencies of 1.07×10^{-7} and 1.5×10^{-5} at $P_{avg} = 73.7$ mW, higher harmonic efficiencies ~0.01% and 0.1% for SHG and THG, respectively, can be achieved by tuning the compression through input pulse chirp control, as seen from Figs. 5(d)–5(f). For CSHG, we achieve a maximum efficiency of 9.4×10^{-4} in our experiments, assuming THG as the pump. We attribute this large efficiency of CSHG compared to SHG to the $1/\lambda^3$ dependence of γ_{SH} and better phase matching due to the availability of a large number of modes around 260 nm [see Fig. 2(a)].

The efficiency of the harmonic signals can be further improved by having a waveguide with multiple optical modes at the harmonic frequency [see Fig. 2(a)]. The availability of a large number of modes can facilitate better phase matching, access to modes with better overlap with the pump mode, and coupling of pump to many modes, all of which may compensate for the overlap integral-induced reduction in efficiency resulting from signal being in higher-order mode [24]. By carefully drawing the taper waist, we can tune the wavelengths of these modes. A large spectral bandwidth of the pump pulse will also help in phase matching multiple harmonic modes.

To the best of our knowledge, this is the first report of the translation of an IR frequency comb at 1550 nm to the wavelength region covering deep UV to NIR in a single device. In [6], a narrowband (<1 nm) SHG was observed in a periodically poled silica fiber (PPSF) using a low repetition rate (20 kHz) nanosecond duration pulsed signal at 1550 nm with ~μJ pulse energy. The SHG signal from PPSF was then used to obtain a 260 nm signal with an efficiency $\sim 10^{-8}$ through THG in a silica taper [6]. In this work, we achieve a 260 nm signal with 1 nW power and a broad bandwidth of ~80 THz using a pump pulse energy of 1 nJ. The deep UV efficiency $\sim 10^{-3}$, which is calculated using the THG signal as the pump, in our demonstration is 5 orders larger. Compared to previous results, this setup shows a higher efficiency due to large spectral bandwidth and higher peak power. From the measured optical spectra at $P_{avg} = 73.7$ mW, we obtain a 3 dB bandwidth of 84.3, 14.61, and 10.84 THz for the combs centered at 260, 520, and 780 nm, respectively. Using the measured 3 dB spectral widths of different harmonics and MLL repetition rate, we obtain the number of comb lines to calculate the number of photons per comb line per second. For deep UV, we obtain 1500 photons (N^{DUV}_{photon}) per comb line per second, which is sufficient for atom spectroscopy using single-photon detectors [1]. For photon-level spectroscopy, light–atom interaction can be further enhanced by copropagating a CW laser with the mode-locked pulses in the nanowire and trapping the atoms in the evanescent field of the CW laser [25–27]. The number of photons per comb line per second for SHG (N^{780}_{photon}) and THG (N^{520}_{photon}) are 3×10^5 and 18×10^6, respectively. Further dispersion engineering to reduce the pulse walk-off between the pump and different harmonics, use of long-length nanowires, and increasing pulse energies from the nanojoule level, which is used in our demonstration, to ~ tens of nannojoules will result in larger powers and efficiency for different harmonics. Figure 2(a) shows that the nanowire has multiple modes around the harmonic frequencies, which can enhance the efficiency of deep UV generation by coupling to a mode that reduces the overall phase mismatch. Further, controlling the spectral bandwidth of the pump pulse so that multiple harmonic modes fall in the phase-matching bandwidth will also enhance the efficiency.

C. RF Signal Analysis

To verify the translation of the IR frequency comb to visible, we measure the RF spectrum of the MLL pump and the THG signal using an RFSA and optical filters, which are used to filter the pump and other harmonics. Figures 6(a) and 6(b) show the RF spectrum for the THG and the MLL pump, respectively. The beat signals at the multiples of 82 MHz in the THG and MLL RF spectrum demonstrate that the comb at 1560 nm is translated to 520 nm. The smaller RF components in the pump frequency comb [Fig. 6(b)] arise inside the erbium-doped fiber (EDF) of the MLL. Higher noise floor and small bandwidth (150 MHz) of the visible photodetector increase the noise floor and limit the number of comb lines in the RF spectrum of the THG signal [Fig. 6(a)].

5. DISCUSSION

Trapping of atoms using the evanescent field of nanotapers allows efficient light–matter interaction for ultralow power level spectroscopy and quantum optics [1,25–29]. Many of these applications require frequency combs and ultrashort pulses in the deep UV to NIR wavelength region. Frequency metrology further requires an $f - 2f$ interferometer. Translation of an IR comb in a single nanotaper provides a compact multifunction platform that

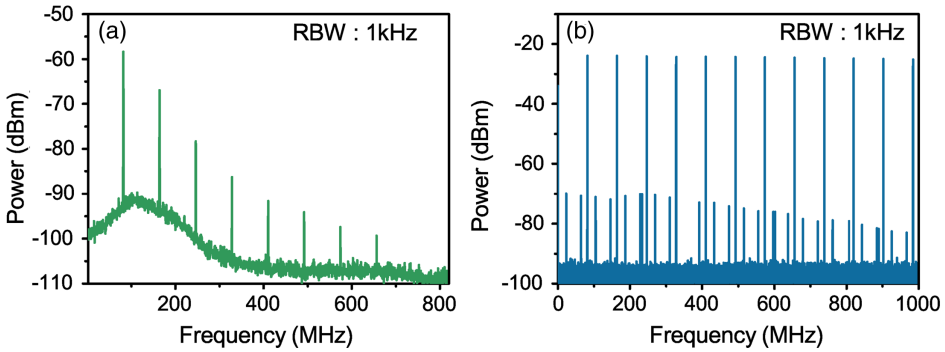

Fig. 6. RF characterization of the THG and pump frequency comb. (a)–(b) RF spectra for THG and pump comb, respectively, showing beat signals at a multiple of 82 MHz, which demonstrate the translation of IR frequency comb to visible.

(i)provides frequency comb from deep UV to NIR, (ii) allows trapping of atoms for quantum optics applications using one wavelength while probing using the other, and (iii) enables $f-2f$ interferometery through cascading of optical nonlinearities, which generate the frequency comb at the second harmonic (260 nm) of the third-harmonic signal (520 nm). For all the frequency combs, the number of photons per comb line are enough to enable photon-level spectroscopy. Since we use only a compact MLL and a nanowire made from an off-the-shelf SMF, our design enables a compact, low-cost, easy-to-realize platform for deep UV to NIR combs. We further show that using chirped pulsed compression, we can achieve higher efficiency at a given pump power through enhanced intensity in the nanowire and compensation of the dispersion-induced phase mismatch through the nonlinearity-induced phase. This will also enable much higher tolerances to the dispersion-induced phase.

Funding. Science and Engineering Research Board (CRG/000993/2019).

Acknowledgment. RP proposed the experiments. AM fabricated the tapers and conducted the experiments and simulations. AM and RP analyzed the data and wrote the paper. RP supervised the project.

Disclosures. The authors declare no competing interests.

Data availability. Data underlying the results presented in this paper are not publicly available at this time but may be obtained from the authors upon reasonable request.

Supplemental document. See Supplement 1 for supporting content.

REFERENCES

1. N. Picqué and T. W. Hänsch, "Photon-level broadband spectroscopy and interferometry with two frequency combs," Proc. Natl. Acad. Sci. USA **117**, 26688–26691 (2020).
2. H. M. Meyer, M. Steiner, L. Ratschbacher, C. Zipkes, and M. Köhl, "Laser spectroscopy and cooling of Yb^+ ions on a deep-UV transition," Phys. Rev. A **85**, 012502 (2012).
3. T. Takaya, C. Su, K. de La Harpe, C. E. Crespo-Hernández, and B. Kohler, "UV excitation of single DNA and RNA strands produces high yields of exciplex states between two stacked bases," Proc. Natl. Acad. Sci. USA **105**, 10285–10290 (2008).
4. M. L. Davenport, S. Liu, and J. E. Bowers, "Integrated heterogeneous silicon/III–V mode-locked lasers," Photon. Res. **6**, 468–478 (2018).
5. P. D. Reid and D. M. Ferrera, *Compact Visible Frequency Combs: The Missing Link in a Vision of Pervasive Quantum Timekeeping* (Engineering and Physical Sciences Research Council, 2016).
6. Y. Wang, T. Lee, F. D. Lucia, M. I. M. A. Khudus, P. J. A. Sazio, M. Beresna, and G. Brambilla, "All-fiber sixth-harmonic generation of deep UV," Opt. Lett. **42**, 4671–4674 (2017).
7. S. Xing, D. Lesko, T. Umeki, A. Lind, N. Hoghooghi, T. Wu, and S. Diddams, "Single-cycle all-fiber frequency comb," arXiv:2104.14649 (2021).
8. N. Koroteev and A. Zheltikov, "Chirp control in third-harmonic generation due to cross-phase modulation," Appl. Phys. B **67**, 53–57 (1998).
9. A. Zheltikov, "Multimode guided-wave non-3omega third-harmonic generation by ultrashort laser pulses," J. Opt. Soc. Am. B **22**, 2263–2269 (2005).
10. A. Zheltikov, "Third-harmonic generation with no signal at 3ω," Phys. Rev. A **72**, 043812 (2005).
11. A. Zheltikov, N. Koroteev, and A. Naumov, "Self-and cross-phase modulation accompanying third-harmonic generation in a hollow waveguide," J. Exp. Theor. Phys. **88**, 857–867 (1999).
12. G. P. Agrawal, *Nonlinear Fiber Optics*, 5th ed. (Academic, 2012).
13. K. Tamura, C. Doerr, L. Nelson, H. Haus, and E. Ippen, "Technique for obtaining high-energy ultrashort pulses from an additive-pulse mode-locked erbium-doped fiber ring laser," Opt. Lett. **19**, 46–48 (1994).
14. V. Mizrahi and J. E. Sipe, "Phenomenological treatment of surface second-harmonic generation," J. Opt. Soc. Am. B **5**, 660–667 (1988).
15. Y. Ohmori and Y. Sasaki, "Two-wave sum-frequency light generation in optical fibers," IEEE J. Quantum Electron. **18**, 758–762 (1982).
16. R. W. Terhune and D. A. Weinberger, "Second-harmonic generation in fibers," J. Opt. Soc. Am. B **4**, 661–674 (1987).
17. D. Z. Anderson, V. Mizrahi, and J. E. Sipe, "Model for second-harmonic generation in glass optical fibers based on asymmetric photoelectron emission from defect sites," Opt. Lett. **16**, 796–798 (1991).
18. R. Stolen and H. Tom, "Self-organized phase-matched harmonic generation in optical fibers," Opt. Lett. **12**, 585–587 (1987).
19. U. Österberg and W. Margulis, "Experimental studies on efficient frequency doubling in glass optical fibers," Opt. Lett. **12**, 57–59 (1987).
20. J. Lægsgaard, "Theory of surface second-harmonic generation in silica nanowires," J. Opt. Soc. Am. B **27**, 1317–1324 (2010).
21. D. Milam, "Review and assessment of measured values of the nonlinear refractive-index coefficient of fused silica," Appl. Opt. **37**, 546–550 (1998).
22. M. I. A. Khudus, T. Lee, T. Huang, X. Shao, P. Shum, and G. Brambilla, "Harmonic generation via $\chi 3$ intermodal phase matching in microfibers," Fiber Integr. Opt. **34**, 53–65 (2015).
23. A. M. Schober, G. Imeshev, and M. M. Fejer, "Tunable-chirp pulse compression in quasi-phase-matched second-harmonic generation," Opt. Lett. **27**, 1129–1131 (2002).
24. T. Lee, Y. Jung, C. A. Codemard, M. Ding, N. G. Broderick, and G. Brambilla, "Broadband third harmonic generation in tapered silica fibres," Opt. Express **20**, 8503–8511 (2012).
25. E. Vetsch, D. Reitz, G. Sagué, R. Schmidt, S. Dawkins, and A. Rauschenbeutel, "Optical interface created by laser-cooled atoms trapped in the evanescent field surrounding an optical nanofiber," Phys. Rev. Lett. **104**, 203603 (2010).
26. S. Spillane, G. Pati, K. Salit, M. Hall, P. Kumar, R. Beausoleil, and M. Shahriar, "Observation of nonlinear optical interactions of ultralow levels of light in a tapered optical nanofiber embedded in a hot rubidium vapor," Phys. Rev. Lett. **100**, 233602 (2008).
27. J. D. Thompson, T. Tiecke, N. P. de Leon, J. Feist, A. Akimov, M. Gullans, A. S. Zibrov, V. Vuletić, and M. D. Lukin, "Coupling a single trapped atom to a nanoscale optical cavity," Science **340**, 1202–1205 (2013).
28. P. Solano, J. A. Grover, J. E. Hoffman, S. Ravets, F. K. Fatemi, L. A. Orozco, and S. L. Rolston, "Optical nanofibers," in *Advances in Atomic, Molecular, and Optical Physics* (Elsevier, 2017), pp. 439–505.
29. A. I. Lvovsky, B. C. Sanders, and W. Tittel, "Optical quantum memory," Nat. Photonics **3**, 706–714 (2009).

202.119.42.173 (ts 2021-09-26 10:56:43)